

# Tropical Cyclone Cloud Image Segmentation by the B-Spline Histogram with Multi-Scale Transforms\*

ZHANG Changjiang<sup>1,2†</sup>(张长江), WANG Xiaodong<sup>2</sup>(汪晓东), and DUANMU Chunjiang<sup>2</sup>(端木春江)

<sup>1</sup> State Key Laboratory of Severe Weather, Chinese Academy of Meteorological Sciences, Beijing 100081

<sup>2</sup> College of Mathematics, Physics and Information Engineering, Zhejiang Normal University, Jinhua 321004

(Received April 30, 2008; revised July 23, 2009)

## ABSTRACT

An efficient tropical cyclone (TC) cloud image segmentation method is proposed by combining the curvelet transform, the cubic B-Spline curve, and the continuous wavelet transform. In order to enhance the global and local contrast of the original TC cloud image, a second-generation discrete curvelet transform is implemented for the original TC cloud image. Based on our prior work, the low frequency components are enhanced by using an incomplete Beta transform and the genetic algorithm in the curvelet domain. Then the enhanced TC cloud image is used to segment the main body of the TC from the TC cloud image. First, pre-processing is implemented by B-Spline curves to the original TC cloud image to remove unrelated small cloud masses. A region of interest (ROI) which includes the main body of TC can thus be obtained. Second, the gray-level histogram of ROI is obtained. In order to reduce oscillations of the histogram, the gray-level histogram is smoothed by cubic B-Spline curves and the B-Spline histogram is obtained. The one dimensional continuous wavelet transform is employed for the curvature curve of the B-Spline histogram. A new segmentation cost criterion is given by combining threshold, error, and structure similarity. The optimally segmented image can be obtained by the criterion in the continuous wavelet domain. The optimally segmented image is post-processed to obtain the final segmented TC image. The experimental results show that the main body of TC can be effectively segmented from the complex background in the TC cloud image by the proposed algorithm.

**Key words:** tropical cyclone cloud image, segmentation, B-Splines, curvelet transform, continuous wavelet transform

**Citation:** Zhang Changjiang, Wang Xiaodong, and Duanmu Chunjiang, 2010: Tropical cyclone cloud image segmentation by the B-Spline histogram with multi-scale transforms. *Acta Meteor. Sinica*, **24**(1), 78–94.

## 1. Introduction

With the improvement in time and spatial resolutions of satellite, the satellite cloud image has become an important tool for monitoring tropical cyclones (TCs). The TC cloud image segmentation is an important issue but is also a difficult one. A complete TC cloud mass includes all kinds of clouds. The TC cloud mass includes different types of clouds in different developing phases. Therefore, it is very difficult to use a proper statistic method to process all kinds of clouds. Currently, no general algorithm suitable for all applications is found. In general, different segmen-

tation approaches are used to segment different kinds of images. In this paper, we aim to segment the main cloud series from a TC cloud image.

Many researchers have done lots of good work in this area. Some researchers have carried out studies to segment a satellite image by using shape (Chehdi and Liao, 1993; Waldemark et al., 2000), colour, texture or region information (Shan et al., 1993; Tateyama et al., 2002). Some researchers have carried out studies to segment a satellite image by using mathematical morphology (Tateyama et al., 2004; Liu et al., 2001, 2004; Wang et al., 2001; Liu et al., 1997; Lopez et al., 2004; Intajag et al., 2006). Many researchers used the

\*Supported by the National Natural Science Foundation of China (40805048), Zhejiang Provincial Natural Science Foundation (Y506203), Shanghai Typhoon Institute /China Meteorological Administration (2008ST01), the State Key Laboratory of Severe Weather/Chinese Academy of Meteorological Sciences (2008LASW-B03), and the Research Foundation of State Key Laboratory of Remote Sensing Science jointly sponsored by the Institute of Remote Sensing Applications of Chinese Academy of Sciences and Beijing Normal University (2009KFJJ013).

†Corresponding author: zcj74922@zjnu.edu.cn.

clustering algorithm to segment a satellite image (Xue et al., 2006; Baraldi and Parmiggiani, 1998; Thitimajshima, 2000; Ooi and Lim, 2006; Rekik et al., 2006). Some other researchers have segmented a satellite image by using the artificial intelligent algorithm (Vannoorenberghe and Flouzat, 2006; Ye et al., 2006; Neaogoe and Fratila, 1999; Shi et al., 2001). Most of the above works are engaged in high resolution satellite images. Segmentation of TC cloud image is very important in weather forecasting, however, relevant research in this respect is little (Liu et al., 2004; Wang et al., 2001; Liu et al., 1997; Lopez et al., 2004; Baraldi and Parmiggiani, 1998). Most of the segmentation methods for TC cloud images are based on intensity or texture of satellite cloud images, without considering the radian information of the TC. Therefore, this may result in inaccurate segmentation for some TC cloud images.

Recently, the multi-scale geometry analysis (MGA) method has been widely used in image processing. Discrete curvelet transform is an efficient MGA method (Jean et al., 2002). It has many advantages compared with the wavelet transform. For example, it has better directional properties. This method has been used widely in image denoising, enhancement, segmentation, fusion, and compression (Long et al., 2005). It is divided into two categories: first-generation curvelet transform and second-generation curvelet transform. The computation burden of the second-generation curvelet transform is less than that of the first-generation.

In this paper, we use the second-generation discrete curvelet transform, an incomplete Beta transform, and the genetic algorithm (GA) to enhance the global and local contrast of an original TC cloud image. The enhanced image is used to segment the main body of the TC. Pre-processing is done to the original TC cloud image to get rid of unrelated small cloud masses. We use the one-dimensional continuous wavelet transform (CWT) and cubic B-Spline curves to segment the pre-processed TC cloud image. Firstly, a B-Spline curve is used to smooth the oscillations of original gray level histogram and the B-Spline histogram is obtained. The curvature curve of the B-Spline histogram is decomposed with the one-dimensional CWT. Secondly, based on our prior work

(Zhang et al., 2007a), an optimally segmented TC cloud image is obtained. A new cost criterion is proposed by combining Jung criterion (Chang et al., 1997) with structure similarity (Wang et al., 2004) to determine the optimal segmentation scale in the CWT domain. Post-processing is implemented to the optimally segmented TC cloud image to obtain the final segmented TC cloud image.

## 2. Pre-processing for TC cloud image

The original TC cloud image may be fuzzy or of bad contrast for various reasons. It is necessary to enhance the contrast of TC cloud image in order to efficiently segment the main body of TC from a satellite cloud image. Based on our prior work (Zhang et al., 2007a), the discrete curvelet transform, the incomplete Beta transform, and the GA are used to enhance the global contrast of the TC cloud image. Let the enhanced TC cloud image be  $\mathbf{G}$  (Zhang et al., 2007a). Median filter is used to suppress the noise in the TC cloud image, thus a filtered image  $\mathbf{M}$  is obtained. Let  $\mathbf{F}$  show the original TC cloud image. In order to enhance the low frequency components of the TC cloud image, a new TC cloud image  $\mathbf{L}$  can be obtained as follows:

$$\mathbf{L}(x, y) = \mathbf{G}(x, y) - \mathbf{F}(x, y). \quad (1)$$

Similarly, in order to enhance the high frequency components of the TC cloud image, another new TC cloud image  $\mathbf{H}$  can be obtained as follows:

$$\mathbf{H}(x, y) = \mathbf{G}(x, y) - \mathbf{M}(x, y). \quad (2)$$

Therefore, an ultimate enhanced TC cloud image  $\mathbf{U}$  can be obtained by

$$\mathbf{U}(x, y) = \alpha \mathbf{L}(x, y) + \mathbf{M}(x, y) + \beta \mathbf{H}(x, y), \quad (3)$$

where  $x = 1, 2, 3, \dots, C$ ;  $y = 1, 2, 3, \dots, R$ . Variables  $C$  and  $R$  respectively represent the columns and rows of the TC cloud image.  $\alpha$  and  $\beta$  are constants which control the enhanced extent for low and high frequency components of the TC cloud image. Here we set  $\alpha = \beta = 1$ .

### 3. The B-Spline histogram

Bezier curve is a kind of parameters curve based on approximation, which was constructed by Bezier in French in 1962 (Sun, 1998). Bezier curve has been used to smooth the histogram of satellite cloud image in our prior research (Zhang et al., 2007a). Bezier curve has many advantages. However, it has two shortcomings: (1) Rank of Bezier curve is determined by the number  $n$  of vertices of characteristic polygon. The ability that the characteristic polygon controls the Bezier curve will become weak when  $n$  is large. (2) Local modification cannot be implemented in Bezier curve, i.e., the whole curve will be influenced if position of one control knob is changed. In 1972, Gordon expanded the Bezier curve. B-Spline function was used to replace Bernstein function. B-Spline curve can improve the defects of the Bezier curve. We use even B-Spline function to smooth the histogram of the pre-processed TC cloud images. Referring to the Bezier curve equation, B-Spline curve which has  $n + 1$  control knots  $P_i$  ( $i = 0, 1, \dots, n$ ) can be written by

$$C(u) = \sum_{i=0}^n P_i N_{i,k}(u), \quad (4)$$

where  $N_{i,k}(u)$  is the base function, and it can be defined as

$$N_{i,0}(u) = \begin{cases} 1, & t_i \leq u \leq t_{i+1} \\ 0, & \text{otherwise} \end{cases} \quad (5)$$

$$N_{i,k}(u) = \frac{(u - t_i)N_{i,k-1}(u)}{t_{i+k} - t_i} + \frac{(t_{i+k-1} - u)N_{i+1,k-1}(u)}{t_{i+k+1} - t_{i+1}} \quad (t_k \leq u \leq t_{n+1}), \quad (6)$$

where  $t_i$  is the knot value, and  $T = [t_0, t_1, \dots, t_{L+2k+1}]$  ( $L = n - k$ ) forms the knot vector of the  $k$ th order B-Spline function. Equation (6) is the even B-Spline function when  $t_{i+1} - t_i = \text{constant}$ . We have to use the discrete matrix form of the B-Spline curve to smooth the histogram of TC cloud images. Here we use cubic B-Spline curve to complete the task. A piece of cubic B-Spline curve can be obtained by extracting neighboring four knots every time from  $n + 1$  control knots  $P_i$  ( $i = 0, 1, \dots, n$ ). The base

function of the cubic B-Spline curve can be written by

$$\mathbf{N}_{i,3}(u) = [N_{1,3}(u) \ N_{2,3}(u) \ N_{3,3}(u) \ N_{4,3}(u)] \quad (7)$$

where

$$N_{1,3}(u) = (1/6)(-u^3 + 3u^2 - 3u + 1), \quad (8)$$

$$N_{2,3}(u) = (1/6)(3u^3 - 6u^2 + 4), \quad (9)$$

$$N_{3,3}(u) = (1/6)(-3u^3 + 3u^2 + 3u + 1), \quad (10)$$

$$N_{4,3}(u) = (1/6)(u^3), \quad 0 \leq u \leq 1. \quad (11)$$

Thus the base function of the cubic B-Spline can be written by the following matrix:

$$\mathbf{N}_{i,3}(u) = (1/6)[u^3 \ u^2 \ u \ 1] \begin{bmatrix} -1 & 3 & -3 & 1 \\ 3 & -6 & 3 & 0 \\ -3 & 0 & 3 & 0 \\ 1 & 4 & 1 & 0 \end{bmatrix}. \quad (12)$$

Two neighboring cubic B-Spline curves can be written by

$$\mathbf{C}_{i,3}(u) = N_{1,3}(u)P_{i-1} + N_{2,3}(u)P_i + N_{3,3}(u)P_{i+1} + N_{4,3}(u)P_{i+2}, \quad (13)$$

$$\mathbf{C}_{i+1,3}(u) = N_{1,3}(u)P_i + N_{2,3}(u)P_{i+1} + N_{3,3}(u)P_{i+2} + N_{4,3}(u)P_{i+3}. \quad (14)$$

Therefore,  $i$ th cubic B-Spline curve can be written by

$$\mathbf{C}_{i,3}(u) = \sum_{j=1}^4 N_{j,3}(u)P_{i+j-2}. \quad (15)$$

The matrix form, corresponding to Eq. (15), can be expressed as

$$\mathbf{C}_{i,3}(u) = (1/6)[u^3 \ u^2 \ u \ 1] \begin{bmatrix} -1 & 3 & -3 & 1 \\ 3 & -6 & 3 & 0 \\ -3 & 0 & 3 & 0 \\ 1 & 4 & 1 & 0 \end{bmatrix} \begin{bmatrix} P_{i-1} \\ P_i \\ P_{i+1} \\ P_{i+2} \end{bmatrix}, \quad u \in [0, 1], \quad (16)$$

where  $i = 1, 2, \dots, n - 2$ . Direct spline interpolation of noisy histogram of the pre-processed TC cloud image may result in a curve with unwanted oscillations. This is particularly bad because the curvature of the curve is important to determine the segmentation thresholds. A better approach is to reduce the degrees of

freedom for the spline and use the method of least squares to fit the spline to the noisy histogram (Hans, 1998). The degrees of freedom are connected to the number of breaks (knots). Spline interpolation uses all data points as breaks, while spline fitting uses a lower number of breaks. The smoothing effect is controlled by the breaks. Breaks are selected independently of data points or as a subset of data points. Details about the fitting spline can be found in Hans (1998).

Let the original thermal image be quantified into  $L$  gray levels. Position of each control knot in the gray level histogram can be written as:  $P_i = (x_i, y_i), i = 0, 1, 2, \dots, L-1$ . Position vector  $C(u)$  can be determined by the  $L$  control points:

$$C(u) = \sum_{i=0}^{L-1} P_i N_{i,3}(u), \quad (17)$$

where  $0 \leq u \leq 1$ . The vector equation in Eq. (17) can be rewritten into two parameter equations about position as follows:

$$x(u) = \sum_{i=0}^{L-1} x_k N_{i,3}(u), \quad (18)$$

$$y(u) = \sum_{i=0}^{L-1} y_k N_{i,3}(u). \quad (19)$$

Curvature of each control point in B-Spline histogram can be obtained by:

$$Cur(t) = \frac{x'(t)y''(t) - y'(t)x''(t)}{(x'(t)^2 + y'(t)^2)^{3/2}}, \quad (20)$$

where  $Cur(t)$  is the curvature at each control point in Bezier histogram;  $x'(t)$  and  $y'(t)$  are the first derivatives;  $x''(t)$  and  $y''(t)$  are the second derivatives.

#### 4. Threshold segmentation by the CWT and the B-Spline histogram

##### 4.1 Region of interest extraction

In order to reduce the computation burden and accurately extract the region of interest (ROI) which includes main body of the TC, it is necessary to discard some small unrelated cloud masses from the TC cloud image. The B-Spline curve is used to complete

the task. It is used to smooth the gray histogram of the pre-processed TC cloud image in order to reduce the unwanted oscillations in the original histogram of the pre-processed TC cloud image. Thus, the B-Spline histogram can be obtained. According to Section 3, the curvature curve of the B-Spline histogram can also be obtained. Peaks of the curvature curve correspond to valleys of the B-Spline histogram. The gray-level values on the valleys of the B-Spline histogram are considered as segmentation thresholds for the pre-processed TC cloud image. A proper threshold has to be selected to segment the pre-processed TC cloud image and discard the small unrelated cloud masses. In general, brightness of the main body of the TC is greater than other unrelated cloud masses in the infrared TC cloud image.

Let  $t_1, t_2, \dots, t_m$  be the segmentation thresholds according to the above method. So we choose the binary threshold as follows:

$$T_r = t_i, \quad i = \text{int}[\eta \cdot m], \quad (21)$$

where  $0 < \eta < 1$  is a constant used to control the binary threshold to obtain a good binary image. In general, the main body of the TC is brighter than other cloud masses in a TC cloud image. Therefore, we set  $\eta = 0.65$  here to obtain a good binary image.

In order to accurately extract the ROI, which contains the main body of TC, color labeling is implemented to the binary image. In general, the main body of TC should have a bigger area and radian than other cloud masses in the satellite cloud image. Therefore, an overall criterion is given as follows:

$$J_i = B_i^\tau \cdot A_i^\xi, \quad (22)$$

$$A_i = \frac{4\pi B_i}{Z_i^2}, \quad (23)$$

where  $Z_i, B_i$ , and  $A_i$  respectively show the perimeter, area, and radian of the  $i$ th region in the binary image of ROI;  $i = 1, 2, \dots, k$  shows the number of regions in the binary image of ROI;  $\tau$  and  $\xi$  are used to control the importance of area and radian in the overall criterion. From lots of experiments, we find that segmentation results are satisfying when  $\tau = 2$  and  $\xi = 1$ .

## 4.2 Segmentation for ROI

Recently, wavelet transform has become a strong analysis tool in the field of signal processing. Wavelet transform can be classified into two categories: continuous wavelet transform (CWT) and discrete wavelet transform (DWT). The DWT is frequently used because it can be constructed by digital filters. Especially, the DWT can construct orthogonal wavelet basis function and has lots of generalized forms. Therefore, the DWT is widely used in code and data compression. Now, most methods based on wavelet transform to detect the singularity of the signal are using discrete orthogonal wavelet transform or spline wavelet. The methods are based on modular maximum values and zero cross points. Although lots of methods have been proposed to detect the singularity of the signal, their common disadvantage is that the ability to detect faint signal is weak. This is determined by DWT inherent properties. In comparison, the CWT has a bigger advantage than that of DWT in this respect. In this paper, we will use CWT to detect peaks location of the B-Spline histogram of the pre-processed typhoon cloud image so as to well segment the ROI.

The curvature curve of the B-Spline histogram can be obtained by the method described in Section 3. Its peak corresponds to valley in the B-Spline histogram. If it is used directly to determine the segmentation threshold, it will result in worse segmentation because it can only reflect the approximate changes at each control point in the B-Spline histogram. The curvature curve of the B-Spline histogram is decomposed by one-dimensional CWT to accurately segment the TC cloud image. Approximate signal and detail signal can be obtained after decomposition. We will focus on detail signal because it reflects the tiny change at each control point in the B-Spline histogram. Once gray levels, which correspond to peaks, are determined by detail signal at all scales, segmentation threshold can be determined. Gray levels which correspond to valleys between adjacent peaks are considered as quantity gray levels.

We use the method in Zhang et al. (2007a) to obtain a series of dualities  $(T_j^s, Q_j^s)$ ,  $s = 1, 2, \dots, S$ ,

and  $j = 0, 1, 2, \dots, N^s$ ; where  $T_j^s$  and  $Q_j^s$  respectively show the segmentation threshold and quantity gray level corresponding to the peak  $j$  at the scale  $s$ . Let  $X_{\min}$  and  $X_{\max}$  be the minimum and maximum of gray levels in the original image.  $\mathbf{X}(i, j)$  shows the gray-level value at the location  $(i, j)$  in the original image, and  $\mathbf{Y}(i, j)$  indicates the gray-level value at the location  $(i, j)$  in the segmented image. We can segment the thermal image by:

$$\mathbf{Y}(i, j) = \begin{cases} X_{\min}, & X_{\min} \leq \mathbf{X}(i, j) \leq T_0^s, \\ Q_1, & T_0^s \leq \mathbf{X}(i, j) \leq T_1^s, \\ \vdots & \\ X_{\max}, & T_{N^s}^s \leq \mathbf{X}(i, j) \leq X_{\max}. \end{cases} \quad (24)$$

In general, the segmentation result will be closer to the original image when the number of selected thresholds is large. However, this is not what was expected because the segmented result should be more compact so that the subsequent high-level image analysis can be executed efficiently. On the other hand, if the number of selected thresholds is not sufficient, this will result in under-segmentation, and some important features or objects will merge with the background or other irrelevant objects. Therefore, a compromise is needed to solve the above two extreme cases. Here, we propose a cost criterion by combining Jung criterion (Chang et al., 1997) with structure similarity of image (Wang et al., 2004):

$$Cost = \lambda \cdot \sqrt{e} + (1 - \lambda) \cdot N_T \cdot S, \quad (25)$$

where

$$e = \frac{\sum_{i=1}^R \sum_{j=1}^C |\mathbf{X}(i, j) - \mathbf{Y}(i, j)|}{R \cdot C}, \quad (26)$$

$$S = \frac{S_{XY}}{S_X \cdot S_Y},$$

$$S_{XY} = \frac{\sum_{i=1}^R \sum_{j=1}^C [\mathbf{X}(i, j) - \mu_X] \cdot [\mathbf{Y}(i, j) - \mu_Y]}{R \cdot C}, \quad (27)$$

$$S_X = \frac{\sum_{i=1}^R \sum_{j=1}^C |\mathbf{X}(i, j) - \mu_X|}{R \cdot C},$$

$$S_Y = \frac{\sum_{i=1}^R \sum_{j=1}^C |\mathbf{Y}(i, j) - \mu_Y|}{R \cdot C}, \quad (28)$$

where  $Cost$  is cost function;  $e$  is segmentation error;  $R$  and  $C$  are the height and width of original image.  $\mu_x$  and  $\mu_y$  respectively show the mean value of  $\mathbf{X}$  and  $\mathbf{Y}$ .  $N_T$  is the number of segmentation thresholds;  $\lambda$  is weight factor ( $0 < \lambda < 1$ ), which is used to adjust the importance ratio of both factors above. Based on the above cost criterion, the optimal segmentation scale is the one that results in the lowest cost. According to Zhang et al. (2007a), the segmentation is good when  $\lambda = 0.55$ .

### 4.3 Post-processing of the segmented cloud image

Some undesired small cloud masses will affect the center location or cloud tracking when only the CWT-segmentation method is used to segment the TC cloud

image. Therefore, we have to get rid of them. We employ the method in Section 4.1 to obtain multi-thresholds for post-processing of the segmented TC cloud image. Let  $\{\delta_1, \delta_2, \dots, \delta_m\}$  be the segmentation thresholds according to the method in Section 4.1. So we choose the binary threshold as follows:

$$\delta_0 = \delta_i, \quad i = \text{int}[\rho \cdot m], \quad (29)$$

where  $0 < \rho < 1$  is a constant used to control the binary threshold to obtain a good binary image. In general, the main body of the TC is brighter than other cloud masses in a TC cloud image. Therefore, we set  $\rho$  according to Table 1 to obtain a good binary image.

**Table 1.**  $\rho$  values in different contrast types of TC cloud images

Contrast type	GGLD	PD	MD	MDS	MBS	MB	PB
$\rho$	0.65	0.70	0.75	0.80	0.80	0.85	0.90

Note: GGLD (good gray-level distribution), PD (particular dark), MD (medium dark), MDS (medium dark slightly), MBS (medium bright slightly), MB (medium bright), and PB (particular bright) respectively show seven contrast types of the original TC cloud image.

The seven types of contrast in Table 1 were given in Zhang et al. (2007b). The binary image is labeled using the 8-neighbour method. According to Eq. (22), the main body of the TC cloud image (MBOTCCI) is selected from the labeled image. The final segmented image can be obtained by replacing the pixels in the MBOTCCI with the gray-level values of the original TC cloud image.

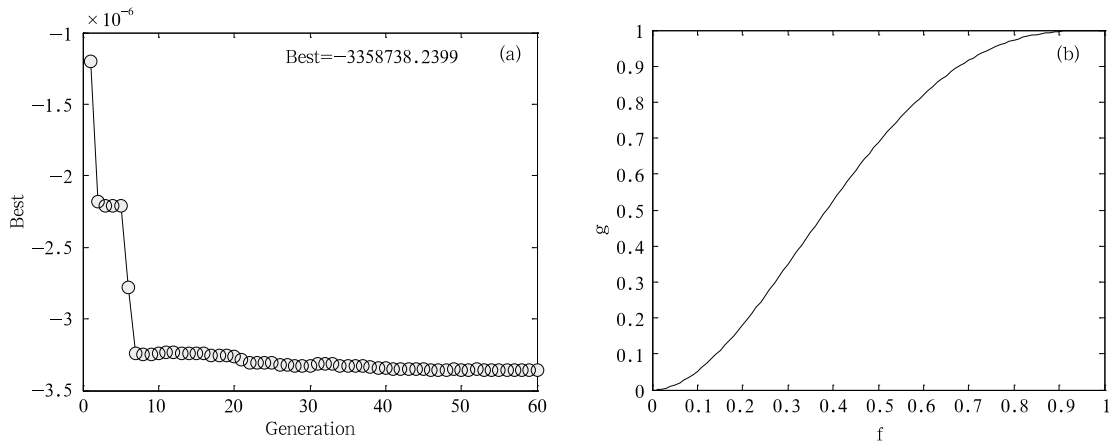
## 5. Experimental results

Lots of experiments have been done to verify the proposed approach. Here only seven segmentation examples are given. The size of the experimental TC cloud image is  $512 \times 512$ . We select morlet wavelet as mother wavelet in the experiments. The original TC image is decomposed into seven levels by the one-dimensional CWT. Figure 1 shows evolution curves of the GA and the incomplete Beta transform ( $a = 1.9983$ ,  $b = 3.0013$ ), where  $a$  and  $b$  are respectively used to control the curve shape of Fig. 1b. Figure 1b is used to enhance the global contrast in Fig. 2a. According to Zhang et al. (2007b), we know that the

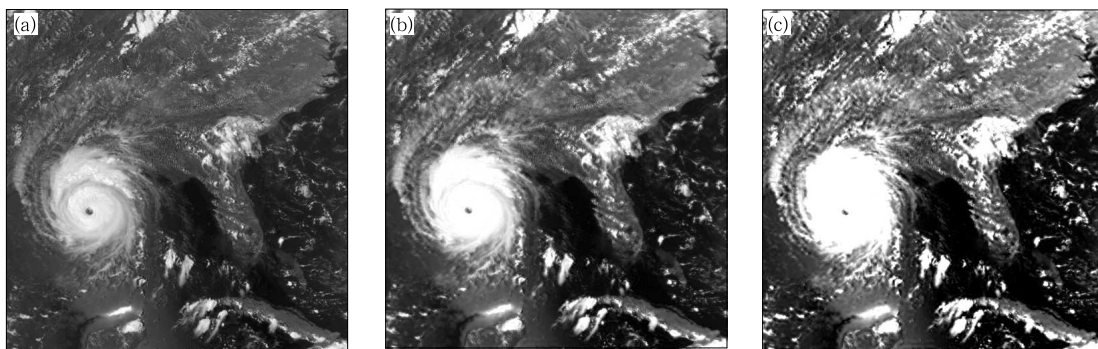
type of contrast in Fig. 2a is ‘‘MDS’’. Therefore  $\rho$  is set as 0.8 in Eq. (29). Figure 2 shows the NOAA-11 cloud image of hurricane ANDREW that occurred on 25 August 1992, in comparison with a directly enhanced image (only based on the method of Zhang et al. (2007a)) and a final enhanced one. From Fig. 2b, we can see that the global contrast of the original typhoon cloud image is well enhanced. According to Fig. 2c, the global and local contrast of the original typhoon cloud image are well enhanced.

Figure 3 shows the histogram of final enhanced typhoon cloud image and its B-Spline histogram. From Fig. 3b, we can see that the oscillations in the histogram of the final enhanced typhoon cloud image has been greatly reduced.

Figures 4a-d show the extraction procedure of the ROI. Figure 4a is a binary image obtained using the method in Section 4.1. Figure 4b represents the labeled image. Figure 4c shows the region whose area is the biggest in Fig. 4b. Figure 4d is the ROI which is obtained by replacing Fig. 4c with the original typhoon cloud image. From Fig. 4, we can see that most of small unrelated cloud masses are reduced and the



**Fig. 1.** Evolution curves of the genetic algorithm (a) and the incomplete Beta transform (b).



**Fig. 2.** Cloud images of Hurricane ANDREW (1992) (a), directly enhanced one (b), and final enhanced one (c).

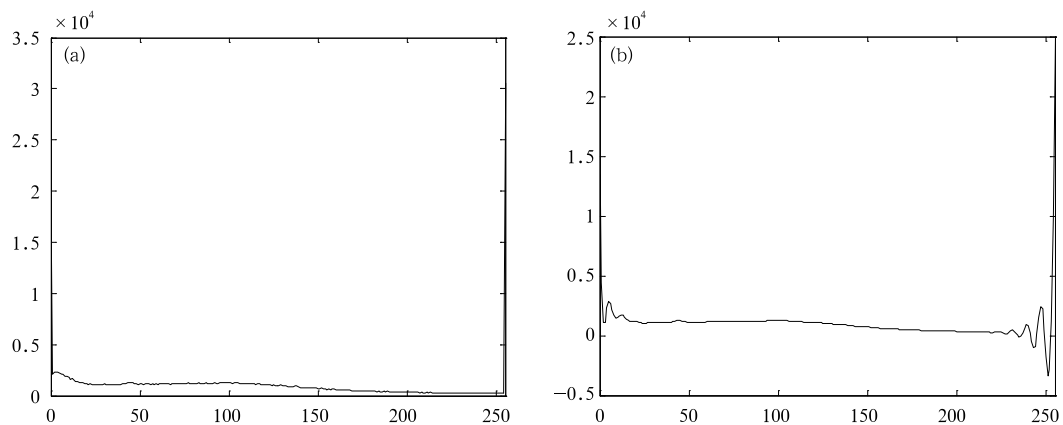


**Fig. 3.** Histogram of final enhanced cloud image (a) and its B-Spline histogram (b).

main body of the typhoon is segmented from the original typhoon cloud image.

Figure 5 shows the histogram of ROI and its curvature curve. From Fig. 5, we can see that there are many undesired peaks in Fig. 5b, which will result in a bad segmentation for the typhoon cloud image. Fig-

ure 6 shows the B-Splines histogram of ROI and its curvature curve. From Fig. 6b, we can see that many undesired peaks have been reduced, which results in a good segmentation for the typhoon cloud image.

In order to accurately detect the locations of

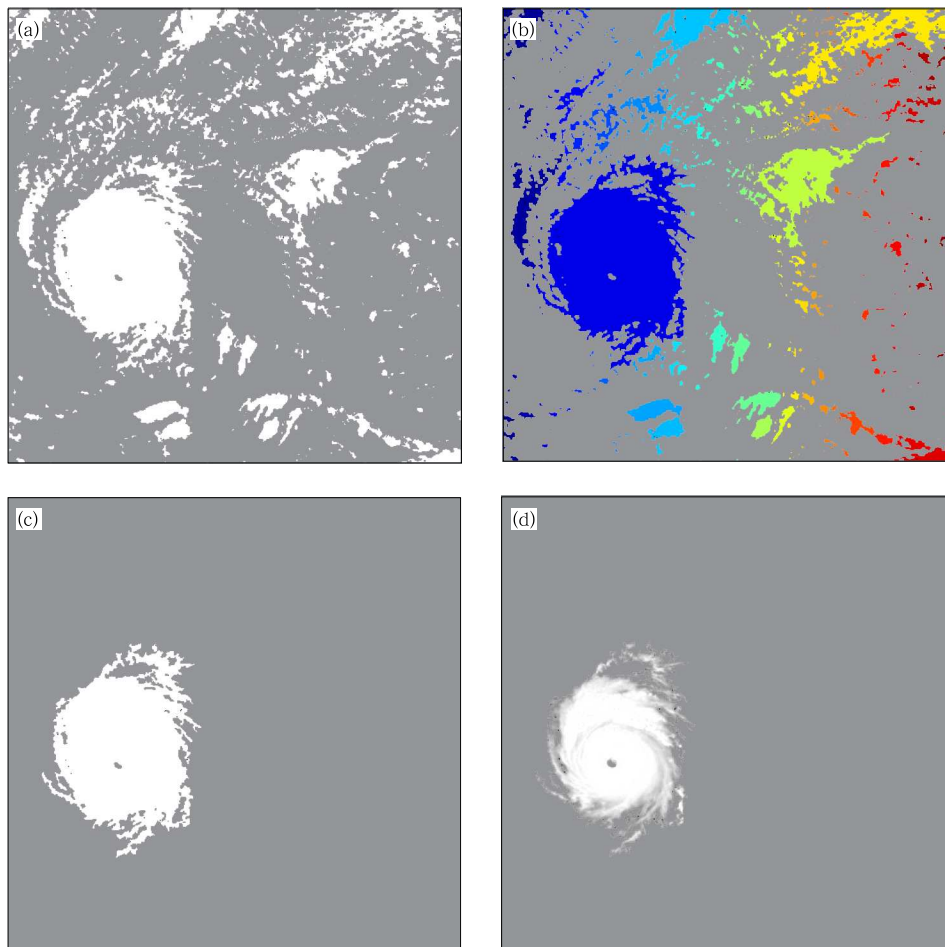


Fig. 4. ROI extraction procedure.

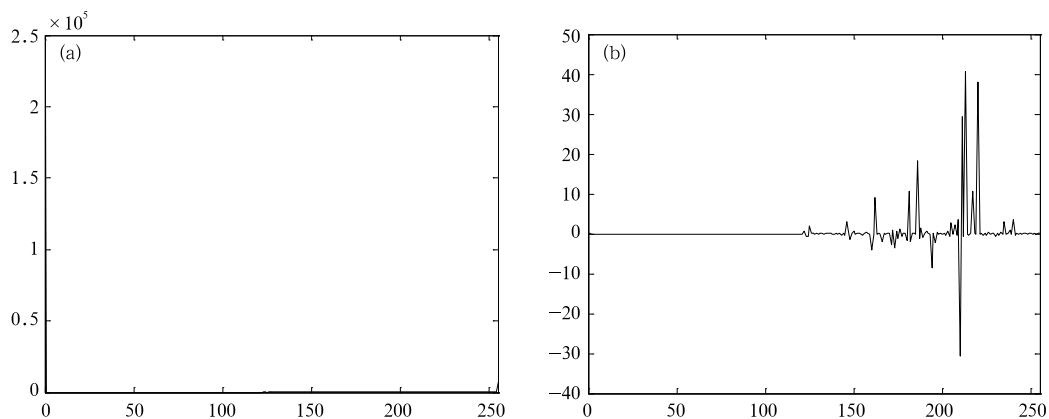


Fig. 5. Histogram of ROI (a) and its curvature curve (b).

peaks and valleys in the curvature curve, the one-dimensional CWT is used to analyze the curvature curve at different scales. Figures 7a-f show the continuous wavelet coefficients of the curvature of the B-

Spline histogram in Fig. 6b. From Fig. 7, it can be seen that fewer and fewer peaks and valleys appear with the scale increasing.

According to Figs. 6 and 7, the gray-level value

corresponding to peaks of the curvature curve is selected as the segmentation threshold. The gray-level value corresponding to valleys of the curvature curve is selected as the quantity gray-level value. We can obtain a group of positions of peaks in Table 2. According to the values, we can segment the main body of the typhoon cloud from the whole typhoon cloud image.

Figures 8a-f respectively represent segmentation results at different scales. The difference between the original cloud image and the segmented cloud image is very small when the segmentation scale is small. This belongs to under-segmentation, and it is obvious in Fig. 8a. The difference becomes bigger when the segmentation scale is increased. This will result in over-segmentation if the segmentation is too big. Some important information has been lost. For example, the structure of the center dense cloud region of the typhoon cloud series is merged into the other cloud masses. We only give 6 segmentation images at 6 scales because Scale 7 is the same as Scale 6.

We use Eq. (25) to determine the optimal segmentation scale. The segmentation cost at different scales is 87.9342, 53.1437, 39.2605, 29.5429, 24.0478, 18.4935, and 18.4935, respectively. Figure 9 shows the segmentation cost curve at different scales. From Fig. 9, we find that the segmentation cost will not decrease after Scale 6. Therefore, we select Scale 6 or Scale 7 as the optimal segmentation scale.

We use the method in Section 4.3 to post-process the optimally segmented image (Fig. 8f). Figure 10 shows histogram and B-Splines histogram of the optimally segmented image.

Figure 11a shows a binary image obtained by the method in Section 4.1. Figure 11b shows the labeled image using the eight-neighbor method. Figure 11c represents the binary image of the TC, which is obtained by the method in Section 4.3. Figure 11d is the final segmentation image. In order to show the efficiency of our algorithm, we compared our algorithm with the Qi method (Qi et al., 2000) and the Olivo method (Olivo, 1994). Figures 11e and 11f respectively represent the segmentation results by the Qi

**Table 2.** Peak positions at all scales

Scale 6	Scale 5	Scale 4	Scale 3	Scale 2	Scale 1
1	1	1	1	1	1
30	15	15	12	12	9
44	30	30	15	15	12
57	44	44	22	22	15
85	57	57	30	30	17
114	70	70	44	38	20
129	85	85	52	44	22
143	93	93	57	52	25
157	114	100	65	57	28
166	129	114	70	65	30
194	143	129	85	70	33
210	157	143	93	78	36
227	166	157	100	85	38
255	194	166	114	93	41
	203	185	129	100	44
	210	194	138	114	46
	227	203	143	129	49
	255	210	157	138	52
		219	166	143	54
		227	172	149	57
		238	185	157	60
		255	194	162	62
			203	166	65
			210	172	70
			219	185	78
			227	191	85
			238	194	93
			243	200	100
			255	203	106
				210	114
				214	122
				219	129
				222	138
				227	143
				233	149
				238	154
				243	157
				249	162
				255	166
					172
					177
					185
					191
					194
					198
					200
					203
					206
					210
					214
					217
					219
					222
					227
					230
					233
					235
					238
					241
					243
					246
					249
					251
					255

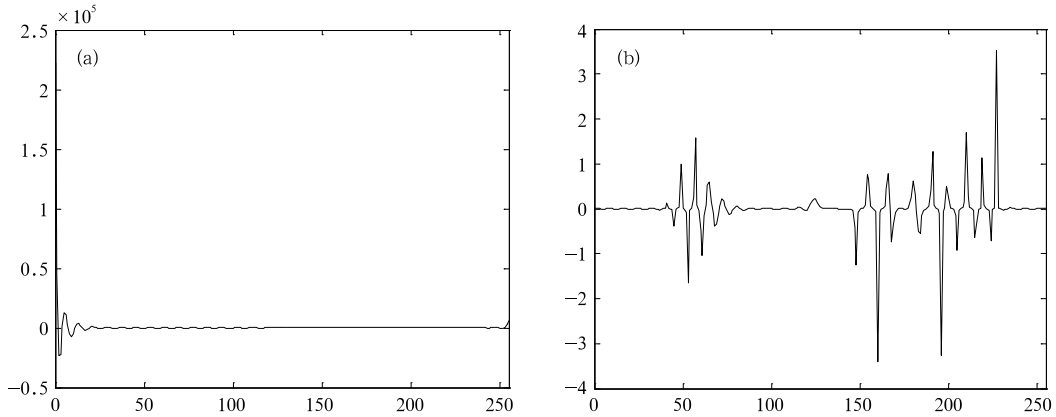


**Fig. 6.** The B-Spline histogram of ROI (a) and its curvature curve (b).

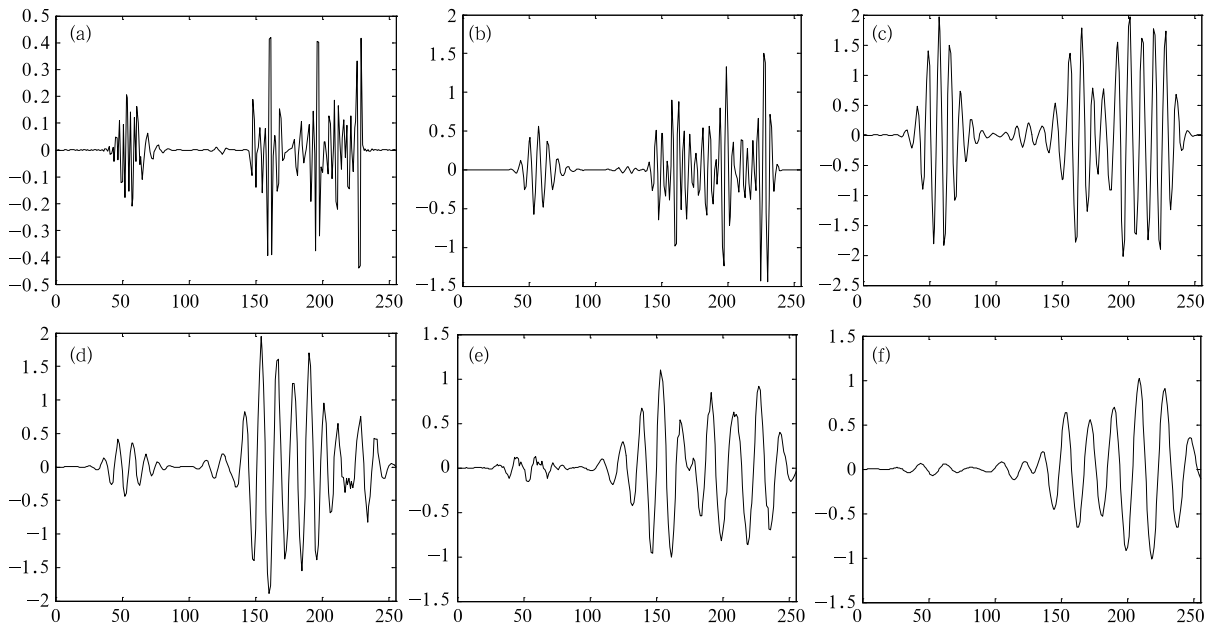


**Fig. 7.** CWT coefficients of the B-Spline curvature curve at Scales 1 (a), 2 (b), 3 (c), 4 (d), 5 (e), and 6 (f).

method and the Olivo method. It is obvious that the Qi method results in over-segmentation. The Olivo method can segment most cloud series of the typhoon; however, there are some undesired small cloud masses in the segmented cloud image. Compared with the Qi and the Olivo methods, the main body of the typhoon cloud can be well segmented from the typhoon cloud image. From Fig. 11d, it is obvious that the main body of the typhoon has been well segmented from the original typhoon cloud image.

We give six other TC cloud images to verify the efficiency of the proposed algorithm, i.e., Fig. 12a (typhoon SEPAT (0709), 07-08-17-16-IR2, MASAT),

Fig. 13a (07-08-18-02-IR2, MASAT), Fig. 14a (07-08-18-14-IR2, MASAT), Fig. 15a (07-08-19-02-IR2, MASAT), Fig. 16a (07-08-19-12-IR2, MASAT), and Fig. 17a (07-08-15-00-IR2, MASAT). Figures 12–17 show respectively the segmentation results of six above TC cloud images. From Figs. 12–17, we can see that both eyed TC (Figs. 12–14) and non-eyed TC (Figs. 15–17) can be efficiently segmented from the satellite cloud image. The segmented TC is complete and can be used to locate the center of the TC or trace the cloud masses of the TC. The segmented TC is either under-segmentation or over-segmentation. Compared with the Qi method and the Olivo method, the overall

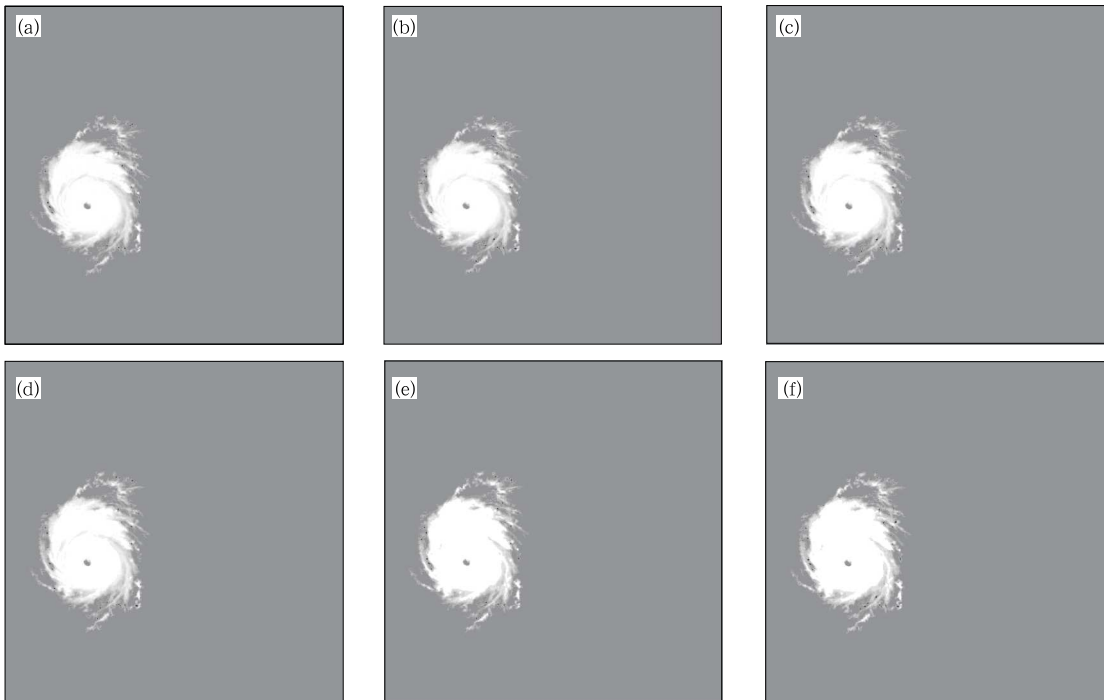


Fig. 8. Segmentation results at different scales from Scales 1 (a) to 6 (f).

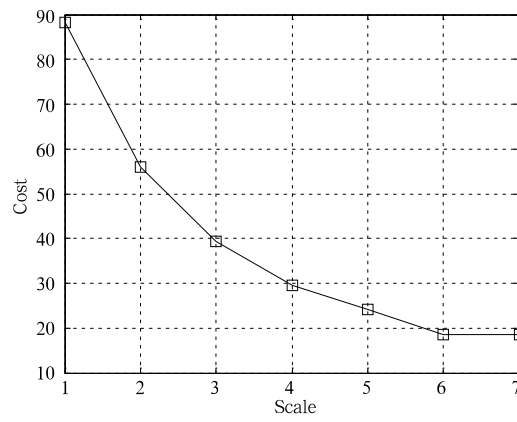


Fig. 9. Segmentation cost at different scales.

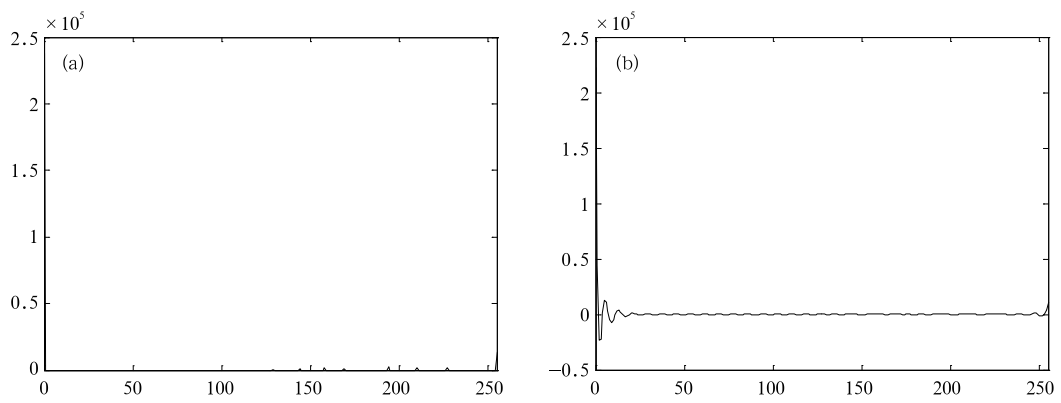


Fig. 10. Histogram (a) and B-Spline histogram (b) of the optimally segmented image.

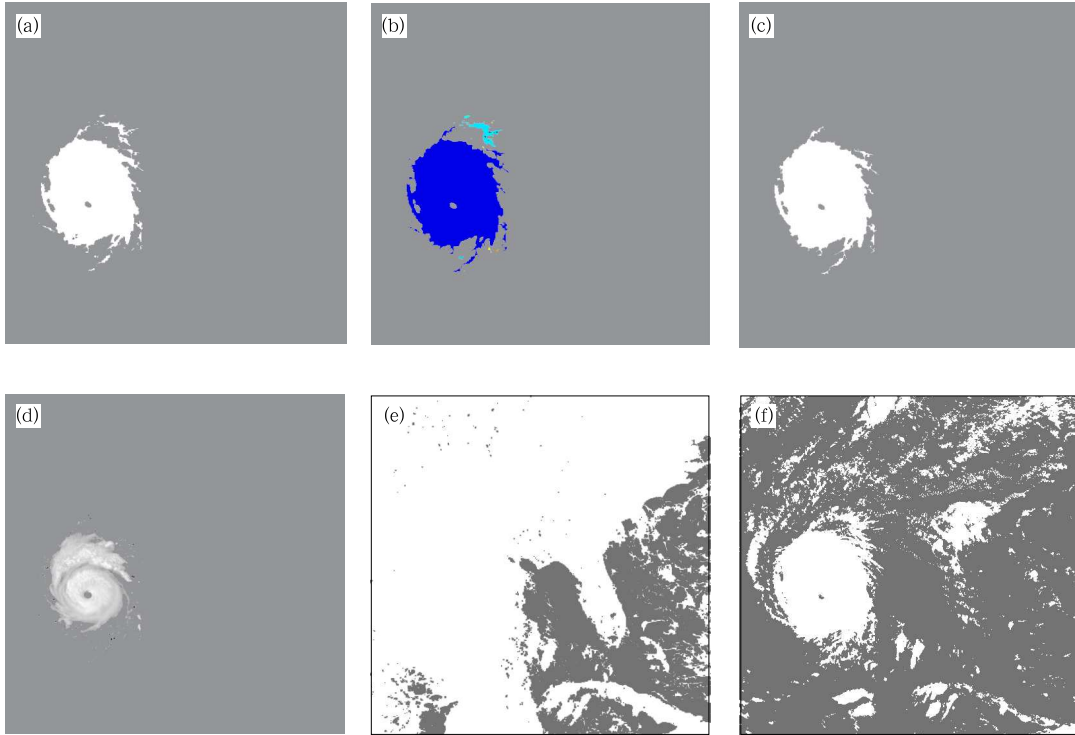


Fig. 11. Post-processing of Fig. 8f.

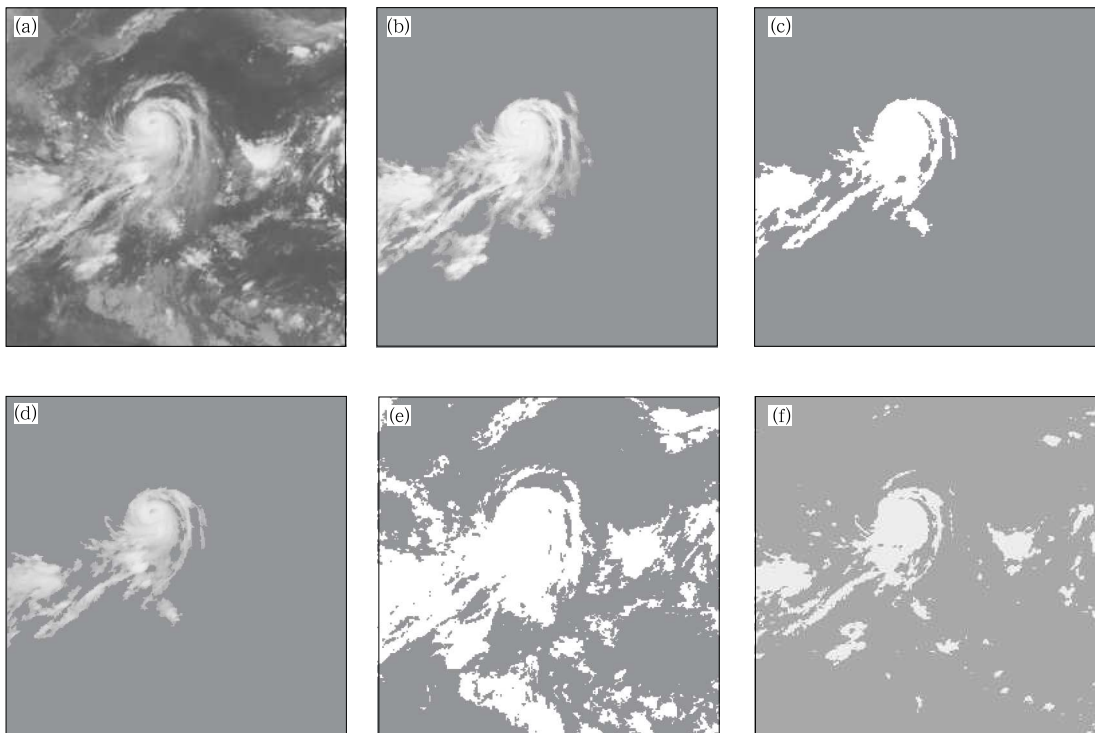


Fig. 12. Segmentation results for TC (07-08-17-16-IR2).

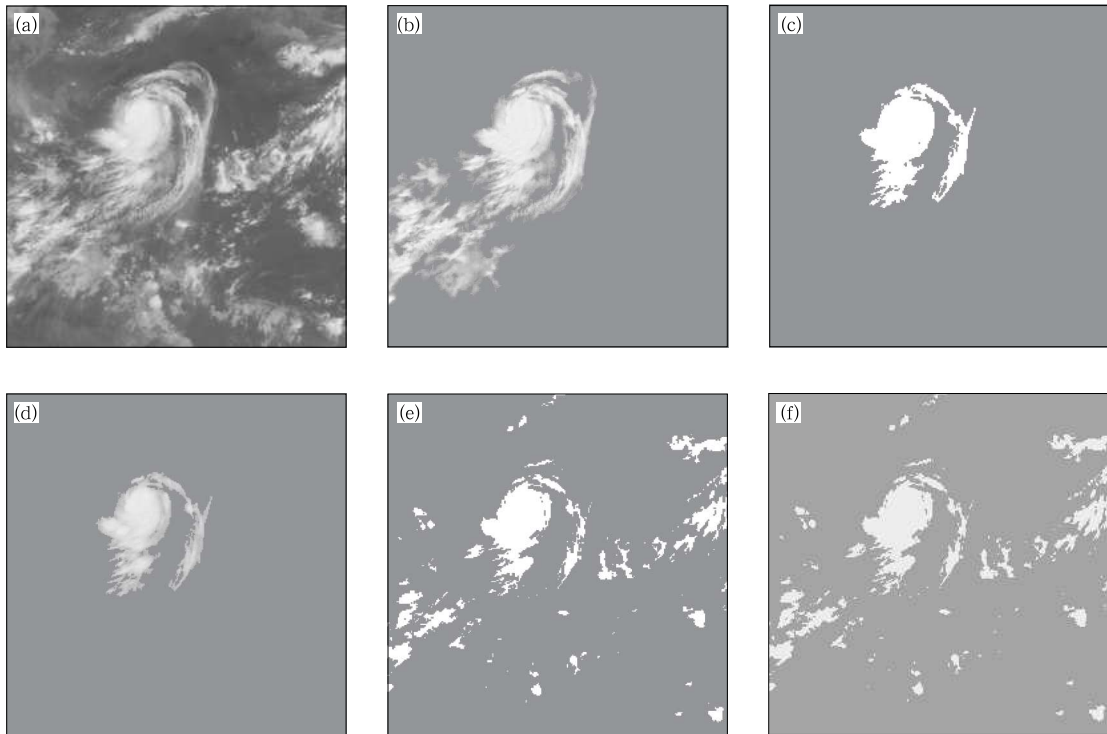


Fig. 13. Segmentation results for TC (07-08-18-02-IR2).

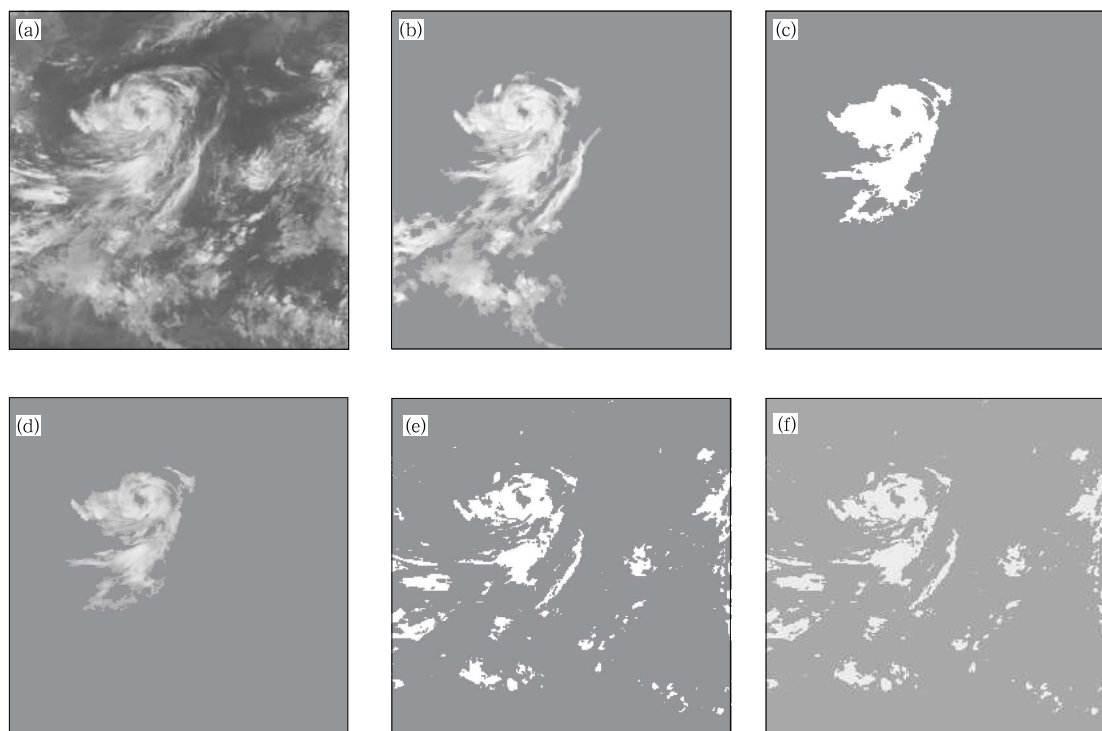


Fig. 14. Segmentation results for TC (07-08-18-14-IR2).

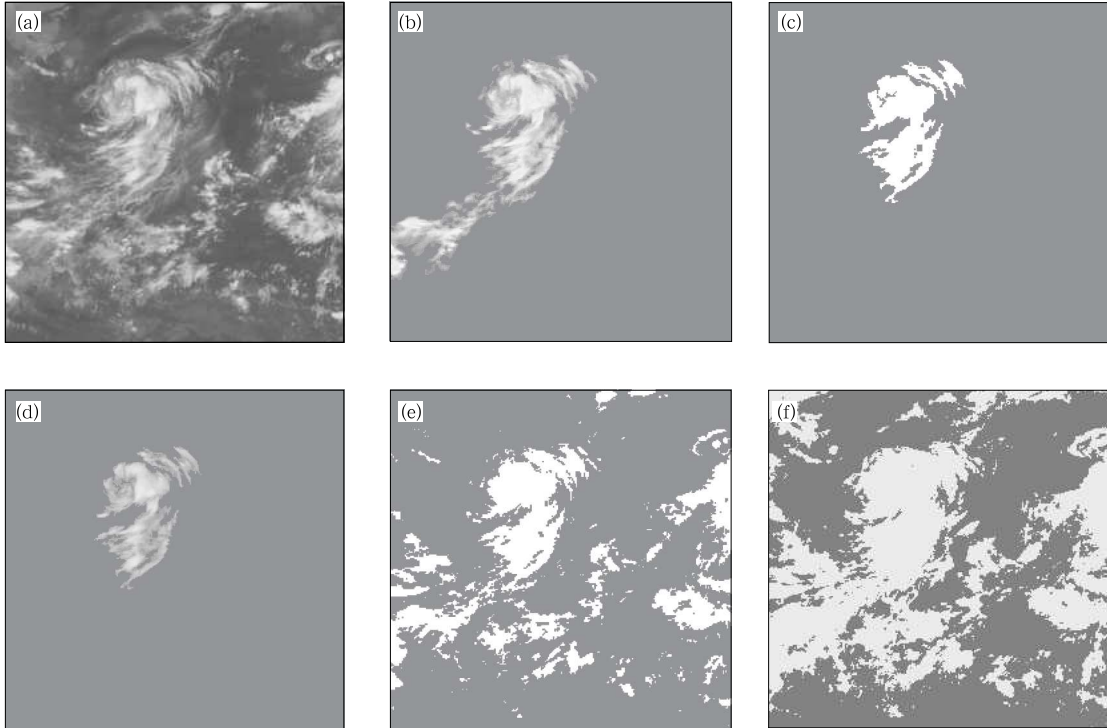


Fig. 15. Segmentation results for TC (07-08-19-02-IR2).

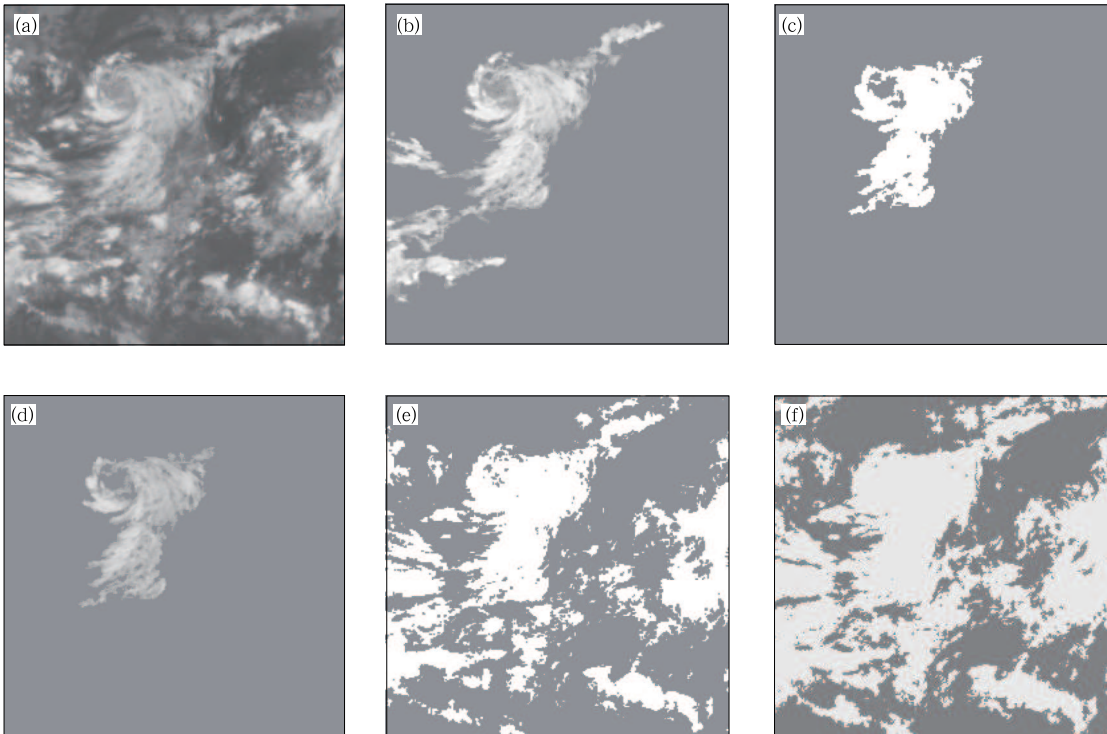
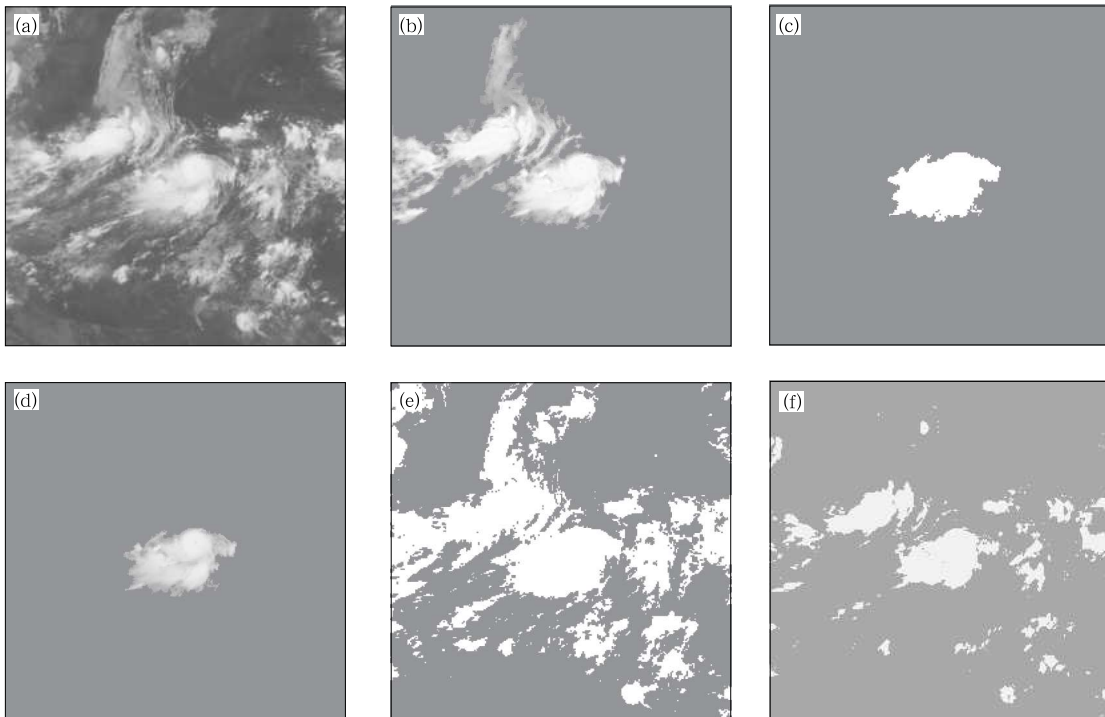


Fig. 16. Segmentation results for TC (07-08-19-12-IR2).

performance of the proposed method is the best.

In order to verify the efficiency of the proposed method, we examined 200 TC cloud images (120 eyed TC cloud images (typhoon) and 80 non-eyed TC cloud images). The 200 TC cloud images are all infrared satellite images, which are obtained by the MTSAT satellite. They include 55 IR1 TC cloud images (07-08-17-00-IR1-07-08-18-21-IR1, 07-08-19-01-IR1-07-08-19-09-IR1), 105 IR2 TC cloud images (07-08-15-00-IR2- 07-08-18-22-IR2, 07-08-19-02-IR2-07-08-19-12-IR2), and 40 IR4 TC cloud images (07-08-17-00-IR4-07-08-17-22-IR4, 07-08-18-02-IR4-07-08-18-18-IR4). Tables 3 and 4 respectively list

the segmentation performance comparison for eyed TCs and non-eyed TCs. According to Tables 3 and 4, we can see that the proposed method has a good segmentation result for eyed TCs. The segmentation results for non-eyed TC cloud images are worse than eyed TC cloud images. This is because eyed TC cloud images have a good helical structure and a clear eye. Compared with two other similar methods, the proposed method can efficiently segment the main body of TC from the satellite cloud image. The accurate segmentation rate of the proposed method is better than the Qi method and the Olivo method.



**Fig. 17.** Segmentation results for TC (07-08-15-00-IR2).

**Table 3.** Segmentation performance for eyed TCs

Segmentation method	Number of samples of eyed TCs	Number of accurate segmentation	Number of wrong segmentation	Accurate segmentation rate
New method	120	115	5	95.83%
Qi method	120	73	47	60.83%
Olivo method	120	77	43	64.17%

**Table 4.** Segmentation performance for non-eyed TCs

Segmentation method	Number of samples of non-eyed TCs	Number of accurate segmentation	Number of wrong segmentation	Accurate segmentation rate
New method	80	72	8	88.57%
Qi method	80	38	42	47.50%
Olivo method	80	33	47	41.25%

## 6. Conclusion

In this paper, we proposed an efficient method to segment TC cloud image by the B-Spline histogram and multi-scale transforms. The oscillations are restrained by B-Spline smoothness. The experimental results show that the new method can efficiently segment TC cloud masses from satellite cloud images. The new method is better than the Olivo method and the Qi method. The Qi method proposed an approach to segment man-made targets based on the curvature of the Bezier histogram. The approach costs less computation time, but, the segmentation result is worse. Some important features or objects will merge with the background or other irrelevant objects. The Olivo method also proposed a segmentation approach based on the dyadic wavelet transform. The approach uses the zero crossing of wavelet signal to determine the segmentation mode. The start, peak, and end positions of modes are adjusted simultaneously by a “coarse-to-fine” adjustment mode. The adjusted modes at the last and the next levels are used to adjust the modes at the current level. Compared with our approach, the Olivo method is very trivial to implement. In the future, we will investigate a method for segmenting TC cloud images by combining texture, direction information of TC with gray level of the TC cloud image.

**Acknowledgements.** The National Satellite Meteorological Center of China Meteorological Administration is acknowledged for providing all the typhoon cloud images in this article.

## REFERENCES

- Baraldi, A., and F. Parmiggiani, 1998: Contextual clustering for satellite image segmentation. Proceedings of the IEEE International Geoscience and Remote Sensing Symposium, Part 5, Seattle, WA, USA, 2041–2043.
- Chang, J. S., H. Y. Mark Liao, and M. K. Hor, 1997: New automatic multi-level thresholding technique for segmentation of thermal images. *Image and Vision Computing*, **15**, 23–34.
- Chehdi, K., and Q. Liao, 1993: Satellite image segmentation using edge-region cooperation. IEEE Pacific Rim Conference on Communications, Computers and Signal Processing, Victoria, BC, Canada, 47–50.
- Hans, B. N., 1998: Cubic Splines. IMM department of mathematical modeling, Technical University of Denmark.
- Intajag, S., K. Paithoonwatanakij, and A. P. Cracknell, 2006: Iterative satellite image segmentation by fuzzy hit-or-miss and homogeneity index. *IEEE Proceedings—Vision, Image and Signal Processing*, **153**, 206–214.
- Jean, L. S., J. C. Emmanunel, and L. D. David, 2002: The curvelet transform for image de-noising. *IEEE Trans. on Image Processing*, **11**, 670–684.
- Liu Kai, Huang Feng, and Luo Jian, 2001: The study on the method of typhoon satellite image segmentation. *Micro-Computer Development*, (1), 54–55. (in Chinese)
- , —, and Kou Zheng, 2004: The segmentation method of typhoon cloud images based on texture and region features. *Computer Engineering and Application*, (33), 219–220. (in Chinese)
- Liu Zhenguang, Lin Kongyuan, Guo Aimin, et al., 1997: Extracting morphological features of satellite images. *Computer Research and Development*, **34**(9), 689–693. (in Chinese)
- Long Gang, Xiao Lei, and Chen Xuequan, 2005: Overview of the applications of curvelet transform in image processing. *Computer Research and Development*, **42**(8), 1331–1337. (in Chinese)
- Lopez, O. E., D. F. Laporterie, and G. Flouzat, 2004: Satellite image segmentation using graph representation and morphological processing. Proceedings of the International Society for Optical Engineering, Bellingham, WA, 104–113.
- Neagoe, V., and I. Fratila, 1999: A neural segmentation of multispectral satellite images. 6th Fuzzy Days. Proceedings of International Conference of Computational Intelligence, Theory and Applications, Dortmund, Germany, 334–341.
- Olivo, J. C., 1994: Automatic threshold selection using wavelet transform. *Graphical Models and Image Processing*, **56**, 205–218.
- Ooi, W. S., and C. P. Lim, 2006: Fuzzy clustering of color and texture features for image segmentation: a study on satellite image retrieval. *Journal of Intelligent & Fuzzy System*, **17**, 297–311.
- Qi, H., W. E. Snyder, D. Marchette, 2000: An efficient approach to segment man-made targets from unmanned aerial vehicle imagery. *Optical Engineering*, **39**, 1267–1274.

- Rekik, A., M. Zribi, M. Benjelloun, et al., 2006: A k-means clustering algorithm initialization for unsupervised statistical satellite image segmentation. First IEEE International Conference on e-Learning in Industrial Electronics, Hammamet, Tunisia, 6.
- Shan, L., M. Berthod, and G. Giraudon, 1993: Satellite image segmentation using textural information, contextual information and map knowledge. International Conference on Systems, Man and Cybernetics. Systems Engineering in the Service of Humans, Le Touquet, France, 355–360.
- Shi, C. X., R. Z. Wu, and X. K. Xian, 2001: Automatic segmentation of satellite images using hierarchical threshold and neural network. *Quarterly Journal of Applied Meteorology*, **12**, 70–78.
- Sun Jiaguang, 1998: *Computer Graphics*. Tsinghua University Press. Beijing, 595 pp. (in Chinese)
- Tateyama, T., Y. W. Chen, X. Y. Zeng, and H. Tamashiro, 2002: A color, texture and shape fusion technique for segmentation of high-resolution satellite images. Knowledge-Based Intelligent Information Engineering Systems and Allied Technologies. Podere d'Ombriano, Crema, Italy, 1167–1171.
- , Z. Nakao, X. Y. Zeng, and Y. W. Chen, 2004: Segmentation of high resolution satellite images by direction and morphological filters. Fourth International Conference on Hybrid Intelligent Systems, Kitakyushu, Japan, 482–487.
- Thitimajshima, P., 2000: New modified fuzzy c-means algorithm for multispectral satellite images segmentation. International Geoscience and Remote Sensing Symposium, Honolulu, HI, USA, 1684–1688.
- Vannoorenberghe, P., and G. Flouzat, 2006: A belief-based pixel labelling strategy for medical and satellite image segmentation. IEEE International Conference on Fuzzy Systems, Vancouver, BC, Canada, 1093–1098.
- Waldemark, K., T. Lindblad, V. Becanovic, and J. L. L. Guillen, 2000: Klinger, P. L. patterns from the sky satellite image analysis using pulse coupled neural networks for pre-processing, segmentation and edge detection. *Pattern Recognition Letters*, **21**, 227–237.
- Wang, P., J. T. Xue, Z. G. Liu, H. Z. Lia, et al., 2001: Self-adaptive segmentation for infrared satellite cloud image. Proceedings of the SPIE-The International Society for Optical Engineering, Wuhan, China, 388–393.
- Wang, Z., A. C Bovik, H. R., Sheikth, et al., 2004: Image quality assessment: from error measurement to structure similarity. *IEEE Transactions on Image Processing*, **13**, 600–612.
- Xue Juntao, Liu Zhengguang, and Wang Ping, 2006: Multiple value self-adapt segmentation of infrared satellite cloud image. *Chinese Journal of Scientific Instrument*, **27**(suppl.), 2166–2167. (in Chinese)
- Ye, Z. G., J. C. Luo, C. P. Bhatta, et al., 2006: Segmentation of aerial images and satellite images using unsupervised nonlinear approach. *WSEAS Transactions on Systems*, **5**, 333–339.
- Zhang, C. J., Duanmu C. J., and Chen H. Y., 2007a: Typhoon image segmentation by combining curvelet transform and continuous wavelet transform. International Conference on Wavelet Analysis and Pattern Recognition, Beijing, China, 1512–1517.
- , X. D. Wang, H. R. Zhang, et al., 2007b: An anti-noise algorithm for enhancing global and local contrast for infrared image. *International Journal of Wavelet, Multi-Resolution and Information Processing*, **5**, 101–112.